Lawrence Berkeley National Laboratory

Title

Custom-designed heat treatment simultaneously resolves multiple challenges facing 3D-printed single-crystal superalloys

Permalink

https://escholarship.org/uc/item/3jc6z57z

Authors

Lin, Sicong

Chen, Kai

He, Weifeng

et al.

Publication Date

2022-10-01

DOI

10.1016/j.matdes.2022.111075

Copyright Information

Peer reviewed

A single annealing treatment simultaneously resolves multiple challenges facing 3D-printed single-crystal superalloys

Sicong Lin[1], Kai Chen[1,*], Yao Li[2], Weifeng He[3], Nobumichi Tamura[4], En Ma[1,*]

1. State Key Laboratory for Mechanical Behavior of Materials, Xi'an Jiaotong University, Xi'an, Shaanxi 710049, P. R. China

2. School of Materials Science and Engineering, Chang'an University, Xi'an, Shaanxi 710064, P. R. China

3. State Key Laboratory for Manufacturing Systems Engineering, Xi'an Jiaotong University, Xi'an, Shaanxi 710049, P. R. China

4. Advanced Light Source, Lawrence Berkeley National Laboratory, Berkeley, CA 94720, USA

E-mail addresses: kchenlbl@gmail.com (K. Chen) and maen@xjtu.edu.cn (E. Ma)

Abstract

Single-crystal Ni-based superalloys are currently the material of choice for turbine blade applications, especially with the emerging additive manufacturing (AM) that facilitates the manufacture/repair of these single crystals. This promising AM route, however, comes with a dilemma: in the fusion and heat affected zones after e-beam or laser induced melting, one needs a solutionizing annealing at a sufficiently high temperature to relieve the residual stresses and homogenize the chemical/microstructure. The solutionizing temperature is usually adopted from the protocol for the cast superalloys, but this heat treatment almost always causes recrystallization and stray grain growth, resulting in a polycrystalline microstructure that degrades the high-temperature mechanical performance. Here we demonstrate a post-printing sub-solvus solutionizing treatment to replace the conventional super-solvus one. The recovery and relatively low temperature diminish the driving force for recrystallization and the movement of stray grain boundaries, without suffocating the chemical/microstructural homogenization thanks to the narrow dendrite width and short element segregation distance. The duration of the sub-solvus solutionizing treatment is optimized to achieve atomic-diffusion mediated chemical homogenization while limiting γ′-particle coarsening in the interdendritic regions. Our solution therefore removes a seemingly formidable obstacle to effective 3D-printing of superalloy single crystal products.

1. Introduction

Ni-based superalloy single crystals are now widely used for turbine blades and vanes in modern aerospace industries [1]. However, making complicated shapes and internal cooling passages [2] in these single crystals has turned out to be much more difficult and expensive, when compared with conventional precision investment casting [3]. In recent years, 3D printing, also known as additive manufacturing, has emerged as a powerful solution to this problem, not only shortening the processing chain and minimizing the waste, but also providing the possibility to repair damaged and/or worn single crystal superalloy parts to extend their service life [4,5]. Rejuvenation (restoration/repair) of microstructures is effective in extending the life of superalloy blades [6], whereas 3D-printing enables precise shape control. However, while crack free superalloy single crystals have been successfully printed [7–9], their microstructure often fails to meet the homogeneity [10] and stability [11] requirements. As a result, it is always necessary to devise a suitable post-printing heat treatment, under either ambient or high pressure [12–14].

To achieve excellent high-temperature performance, Ni-based superalloys incorporate tens of alloying elements, including refractory elements like Re, W and Mo, to form $Ni_3(Al,Ti)$ γ'-precipitates with $L1_2$ structure that are coherent with the solid-solution-strengthened austenitic γ-matrix [15,16]. When produced with the 3D printing approach, the superalloy is deposited layer-by-layer through local melting of the powder feedstock with designed chemical constituents using either a laser or an electron beam heat source [17–19]. Superalloy single crystals are produced under a steep temperature gradient [20], which outperform their polycrystalline counterparts in terms of resistance to creep and fatigue [7,11]. Another advantage brought by the high cooling rate is the refined

62   dendrite structure (several micrometers in width [21]) that provides further strengthening

63   compared to cast superalloys in which the dendrites are usually hundreds of microns wide

64   [22]. Stray grains tend to form on metal surface where the temperature gradient is no longer

65   parallel to the building direction [23,24], thus they are inevitable in 3D-printed superalloy

66   single crystals on both the outer surface of the blades and the inner surfaces of the

67   internal cooling structures [7]. The outer surface can be machined and/or milled to regain

68   the single crystalline structure, but not the inner surfaces of the cooling structures.

69   Fortunately the local service temperature near the inner surfaces is lower than that at the

70   outer surface by several hundred degrees Celsius; the stray grains there are bearable as

71   long as they do not grow much larger into the interior [25,26]. During solidification, the γ-

72   matrix forms first, and ejects the γ'-forming elements into the remaining liquid in-

73   between the dendrites, lowering the liquidus temperature [27]. Once the interdendritic liquid

74   solidifies, its solvus temperature is elevated due to enriched γ'-formers, and as a result the

75   γ'-precipitates in these regions form earlier and grow bigger than those in dendrite cores

76   (DCs). Also, the γ'-precipitate volume fraction and mechanical properties become

77   inhomogeneous across the dendrite width [28–31]. Another issue arising from the rapid

78   cooling rate is the high thermal stress and plastic deformation [32,33]. The stored

79   deformation energy provides the driving force for recrystallization in the bulk, and for

80   stray grain boundary migration near the surface, both of which are detrimental or even

81   disastrous, as they ruin the single-crystalline microstructure desired for retaining high-

82   temperature mechanical properties.

83   From the discussion above, there appear to be four major challenges facing the post-

84   printing heat treatment for 3D-printed superalloy single crystals. Specifically, a

85 successfully customized protocol must be able to (1) *r*elease most of the stored

86 deformation energy, (2) *a*void recrystallization completely, (3) *s*uppress stray grain

87 growth as much as possible, and (4) *h*omogenize the chemical/microstructure distribution

88 to a level comparable with that in cast alloys. From here on these requirements are

89 acronymized as the ***RASH*** challenges. In this paper, we evaluate previously reported heat

90 treatment protocols against these four demands, and then design a novel and yet simple

91 heat treatment, which will be demonstrated to accomplish all the ***RASH*** actions via a

92 single-step solutionizing annealing at sub-solvus temperature prior to aging treatment.

93 This new strategy is conceived based on the following two considerations. First,

94 since the diffusion distance, which is proportional to dendrite width, is greatly reduced in

95 the 3D-printed superalloy due to the fast cooling rate, chemical homogenization at a level

96 similar to the super-solvus solutionizing treatment in the traditional cast products can be

97 achievable with a sub-solvus annealing treatment. Second, by setting the solutionizing

98 temperature above the solvus of the γ'-precipitates in the DCs while below that in

99 interdendritic regions (IRs), the dislocations moving freely in the DCs allow for a speedy

100 recovery. In the meantime, the undissovled γ'-precipitates in IRs would be able to impede

101 the massive motions and interactions of dislocations, nucleation of recrystallized grains,

102 and migration of stray grain boundaries [6]. The success of such a single-step sub-solvus

103 solutionizing treatment will be demonstrated in the following, in two types of superalloy

104 single crystals with different chemical constituents produced using either a laser or an

105 electron beam heat source.

106

107 ## 2. Results

2.1. Necessity for sub-solvus solutionizing heat treatment

Compared to the traditional casting technique, the solidification and cooling processes during 3D printing are faster by several orders of magnitude. In the resultant 3D-printed superalloy, the dendrite width is narrower. The γ′-precipitates are more irregular in morphology, smaller in size, lower in volume fraction, and less stable against temperature excursion [9,34–36]. Despite these differences between casting and 3D-printing, the micro-segregation in the resulting superalloy single crystals is similar. Thus in many cases standard heat treatment protocols of the cast superalloys have been applied to their 3D-printed counterparts, with no modification or just shortening the homogenization treatment duration [13]. As illustrated in the upper panel of Figure 1a, the standard heat treatment of cast superalloys consists of hours of super-solvus solutionizing treatment to homogenize the chemical distribution, followed by a long period of aging treatment to precipitate out, ripen and stabilize the γ′-precipitates [37–39]. However, with such a heat treatment, recrystallization sets in readily from the heat affected zone (HAZ), and the newly formed recrystallization grains as well as the existing stray grains grow big quickly as the grain boundary mobility is high once the specimen is heated above the solvus temperature (Figure 1b). Such observations have been reported previously by many [13,40]. This recrystallization, rendering the single crystal polycrystalline, wastes all the efforts that have been made to achieve the single-crystalline microstructure desired for high temperature mechanical properties. Clearly, the standard heat treatment cannot meet the *RASH* challenges for 3D-printed superalloy single crystals.

Efforts have been made before, to solve the recrystallization issue by applying a pre-solutionizing annealing step to the 3D-printed superalloy single crystals at sub-solvus

6

131   temperature, as shown in the middle panel of Figure 1a. With this step, a large fraction of

132   the stored deformation energy is released prior to solutionizing treatment, taking away the

133   driving force for recrystallization [10]. Afterwards, the standard ageing process is

134   employed, which produces cuboidal γ'-precipitation microstructure indistinguishable

135   from the cast base metal. However, stray grain growth is not precluded during the super-

136   solvus solutionizing treatment, because the migration of high-angle grain boundaries is

137   activated, as indicated by the crystal orientation distribution (inverse pole figure) maps

138   obtained from electron backscatter diffraction (EBSD) scans before and after (Figure 1c)

139   heat treatment of a laser 3D-printed single-crystalline superalloy AM3 specimen. Similar

140   observations have also been recorded in electron beam melted superalloy single crystals

141   (Figure S1). This necessitates a surface subtractive machining process before super-

142   solvus solutionizing heat treatment, to get rid of the seeds of stray grains. Such an extra

143   machining step is not feasible for internal cooling structures, and is in any case time-

144   consuming and costly.

145   Considering that both recrystallization and stray grain growth occur under the

146   precondition of the complete solid-solutioning of γ'-precipitates, we have conceived a

147   different heat treatment protocol. It also consists of two steps of solutionizing and aging

148   treatment, but the solutionizing treatment is carried out at sub-solvus temperature (1270

149    $^{\circ}$C for 30 min in this case) instead of the conventional super-solvus one, as displayed in

150   the bottom panel of Figure 1a. The specimen is exactly the same as the one used for

151   recovery pre-annealing plus super-solvus solutionizing heat treatment, but a pronounced

152   difference in stray grain size is seen in Figure 1d in laser 3D-printed superalloy single

153   crystal AM3. As shown in Figure S1 in the Supporting Information, when the additive

154 manufacturing heat source is changed to electron beam, this method still works well,

155 although here no feedstock is supplied. In other words, combining sub-solvus recovery

156 annealing and super-solvus solutionizing into a single sub-solvus solutionizing treatment

157 meets the "avoid recrystallization" and "suppress stray grain growth" requirements. In the

158 next section, we will further tune the temperature and duration of sub-solvus annealing

159 treatment to homogenize the chemical and microstructure distribution.
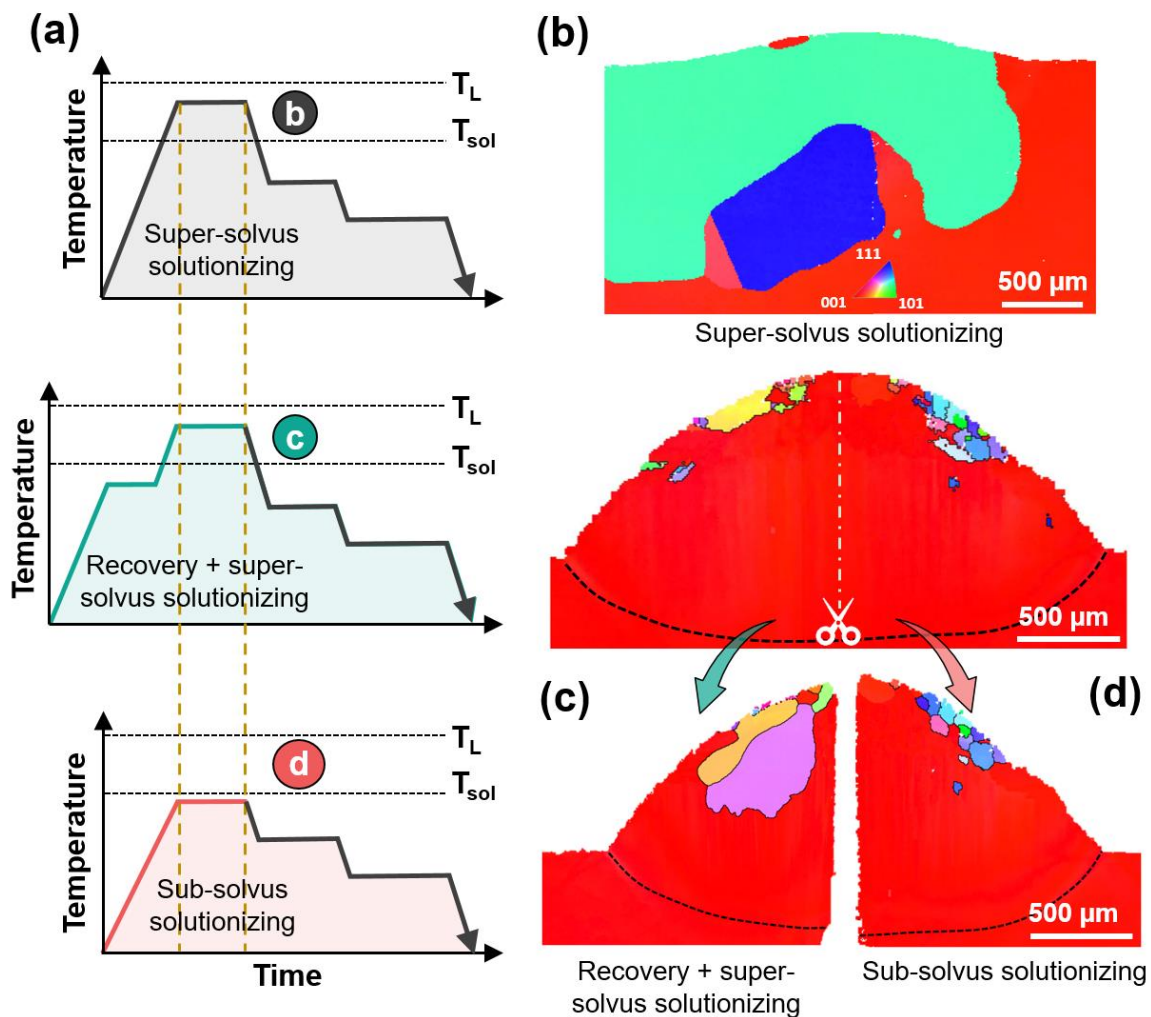
160

161 **Figure 1** Crystal orientation distributions resulted from various heat treatment protocols. (a) Three different
162 heat treatment protocols are considered. (b) Direct super-solvus treatment results in recrystallized
163 microstructure. (c) Recovery (pre-annealing) before super-solvus treatment helps to prevent
164 recrystallization, but stray grains grow bigger. (d) Sub-solvus solutionizing at 1270 $^{\circ}$C eliminates both
165 recrystallization and stray grain growth. T_L and T_{sol} in (a) stand for liquidus and solvus temperatures,
166 respectively. (b-d) are the inverse pole figures obtained from EBSD mapping scanned with 10 μm, 3 μm,
167 and 3 μm step size, respectively.

8

168

169   **2.2. Optimization of annealing temperature and duration**

170   In order to meet all the **_RASH_** requirements, the annealing temperature and duration

171   need to be carefully tailored and optimized. Firstly, the microstructure and residual strains

172   of the as-electron-beam-printed superalloy single crystal are demonstrated in Figure 2.

173   The γ'-particles are tiny (30 - 50 nm in diameter) and irregular in the DCs, whereas in the

174   IRs they appear in almost cuboidal shape with rounded corners and edge length of 70 -

175   100 nm. Based on the contrastive size and shape distribution, the dendrite widths are

176   measured to span from 3 to 10 μm in the fusion zone (FZ). Micro-segregation is clearly

177   seen from the X-ray wavelength dispersive spectra (WDS) maps, showing enriched W in

178   DCs, and Ti and Al in IRs. After electron beam melting, the crystal is riddled with

179   dislocations [34]. The elastic strain associated with these defects is measured using

180   synchrotron based X-ray microdiffraction (μXRD). An area of 80 μm (horizontal) × 1150

181   μm (vertical) across the FZ and the heat affected zone (HAZ) is scanned using micro-

182   focused polychromatic X-ray beam with 2 μm spatial resolution, as marked in Figure

183   S2a, and lattice strain tensor at each scanning position is measured from the Laue

184   diffraction pattern. The equivalent strain ε_{eq} is calculated from the strain tensor, as a

185   representative of the magnitude of the local strain,

186    $\varepsilon_{eq} = \dfrac{\sqrt{2}}{3}\sqrt{(\varepsilon_{xx} - \varepsilon_{yy})^2 + (\varepsilon_{yy} - \varepsilon_{zz})^2 + (\varepsilon_{zz} - \varepsilon_{xx})^2 + 6\varepsilon_{xy}^{\;2} + 6\varepsilon_{xz}^{\;2} + 6\varepsilon_{yz}^{\;2}}$, where ε_{ij} is one of

187   the six strain tensor components. As shown in Figure 2c, the equivalent strain varies

188   pronouncedly in the building direction, but is quite uniform in the horizontal direction; in

189   Figure 2d the average equivalent strain magnitude is therefore plotted as a function of the

190   distance to the melting line. The highest lattice strain, $\sim 4 \times 10^{-3}$, appears near the

191   interface between FZ and HAZ. It decreases gradually into FZ, reaches the minimum

192   value of 1.5×10^{-3} at the position about 350 μm away from the interface, and increases

193   slightly to an almost steady 2×10^{-3}. In the HAZ, the strain distribution is even more non-

194   uniform. The equivalent strain drops to almost zero in a range of 300 μm and then

195   increases back to $\sim 3 \times 10^{-3}$. Although the exact elastic stiffness tensor for AM3 single

196   crystal was not obtained, the peak tensile residual stress is estimated (assuming a

197   modulus of the order ~200 GPa) to be on the order of 0.8 GPa, which is an unacceptably

198   high driving force from the recrystallization and high-angle grain boundary migration

199   points of view. The dislocation density and structure, which is strongly influenced by not

200   only the stress but also the γ/γ' structure, are studied under a transmission electron

201   microscope (TEM). As seen in the bright-field image in Figure 2e, curly dislocations near

202   the melting line, where only tiny γ'-particles exist, are heavily tangled, with a density of

203   approximately 6×10^{14} m^{-2} measured using the line-intercept method [41]. In the HAZ, the

204   density of dislocations is similar to the interfacial area, while the structure is quite

205   different. Because the primary γ'-particles are only partially dissolved, γ-channels are

206   narrower and dislocations are straight and parallel, with pile-ups at the γ/γ' interfaces [42].
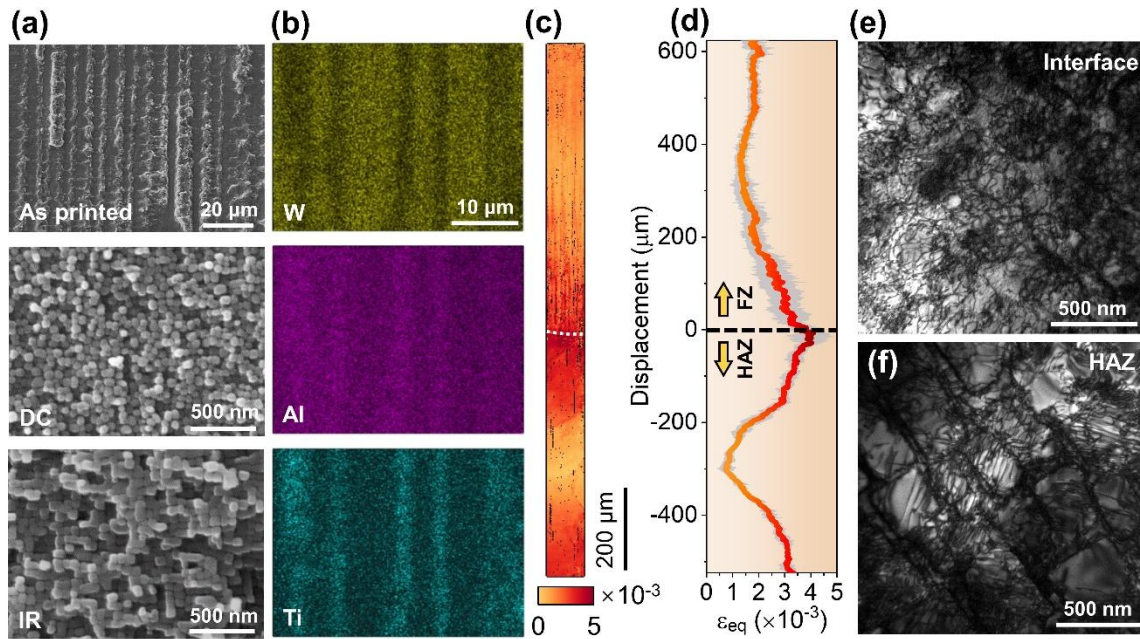
Figure 2 Microstructure of the electron-beam-melted AM3 superalloy single crystal. Distributions of (a) γ′ particles, (b) constituent elemental species, (c-d) equivalent strain, and (e-f) dislocation structures are all inhomogeneous.

Secondly, the solvi of the γ′-precipitates in DCs (T_1) and IRs (T_2) are measured by annealing the specimen at various temperatures for a constant period of time (15 min in this study) and then monitoring the evolution of the SEM image contrast. Once the electron-beam-printed AM3 superalloy was annealed above T_1 (1260 $^{\circ}$C, as displayed in Figure 3a), the γ′-precipitates in the DCs are fully dissolved and then re-precipite as bigger and almost uniform cuboids; in the meanwhile, the γ′-precipitates in the IRs are partially dissolved, resulting in the disappearance of the contrast between DC and IR in some regions. As the annealing temperature goes above T_2 (1280 $^{\circ}$C in this case), the contrast between DC and IR becomes almost homogeneous. These observations suggest that the optimized temperature for the sub-solvus homogenization heat treatment lies between the solvi from 1260 $^{\circ}$C to 1280 $^{\circ}$C.

To guide the selection of the duration time, the classic diffusion equation $d = \sqrt{4Dt}$ is

224 employed. By taking the reported diffusion coefficient D of alloying elements Al, Ti, Ta,

225 and W [43] and setting the diffusion distance d as half of the dendrite width (5 μm), the

226 diffusion time t is calculated for each temperature between 1260 ^{o}C and 1280 ^{o}C. The

227 pace setter, W, migrates the most slowly and the annealing time needs to be longer than

228 13 min when the specimen is heat treated at 1260 ^{o}C, and 10 min for 1280 ^{o}C. For

229 experimental verification of the calculation, the 3D-printed specimen is annealed at 1270

230 ^{o}C for 10 min, ~15% shorter than the calculated time. The chemical composition

231 distribution is found still inhomogeneous, as seen in the WDS map in Figure 3b.

232 Therefore, in the following the annealing time of all experiments is no shorter than the

233 calculated values.

234   The resulted microstructure is sensitive to the annealing temperature. As displayed in

235 Figure 3c, after annealing at 1276 ^{o}C for 10 min, stray grains grow rapidly and

236 overwhelm the whole electron-beam-printed volume. Consequently, the desired annealing

237 temperature should be set below 1276 ^{o}C to fulfill the "suppress stray grain growth" and

238 "avoid recrystallization" requirements.

239   In order to understand how temperature and time influence the homogeneity of the γ′

240 microstructure, identical specimens were sub-solvus solutionizing heat treated at 1270 ^{o}C

241 for 15 min and 30 min, respectively (Figure 3d). For the same period of time (15 min),

242 1270 ^{o}C annealing results in the γ′ microstructure with less contrast than that annealed at

243 1260 ^{o}C; while extending the annealing time (from 15 min to 30 min, or even longer as

244 shown in Figure S3) results in more pronounced contrast and thus microstructural

245 inhomogeneity. Overall, using a shorter time at a higher temperature generates a more

246 homogeneous microstructure.

247   By plotting the observations above into a single "treasure map", we close in on the

248   desired heat treatment protocol, as demonstrated in Figure 3e. In this map, the boundaries

249   are demarcated by the several considerations outlined in the preceding paragraphs.

250   Specifically, the grey areas in this map are not acceptable, as these conditions would

251   subject the alloy to either recrystallization/stray grain growth (increasing in degree when

252   moving to the right), or inhomogeneous chemical composition (increasingly

253   inhomogeneous moving towards the bottom). Only in the blue region, can

254   recrystallization and stray grain growth be successfully prevented, and the chemical

255   uniformity achieved. The bottom right corner of the blue region, indicated by the yellow

256   zone, is the most favorable, because lower temperature together with longer annealing

257   time would be harmful for the γ' particle size homogeneity [44]. Going in this direction

258   leads us to the best spot (1270 $^{\circ}$C for 15 min, as marked by a red star).

259
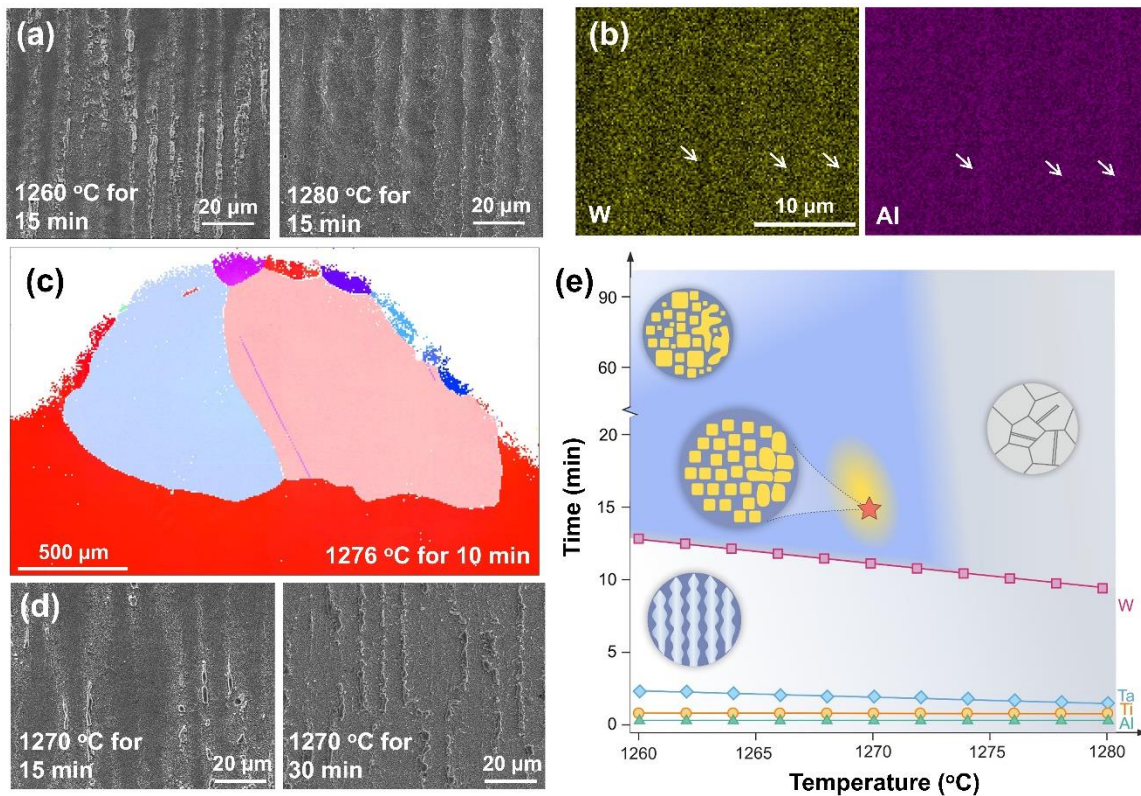
Figure 3 Optimization of heat treatment temperature and time. (a) The microstructure evolution of the γ′-particles in the electron-beam-printed AM3 superalloy, after annealing at 1260 and 1280 $^{\circ}$C for 15 min. (c) is the inverse pole figures obtained from EBSD mapping scanned with 10 μm step size. (d) The contrast of γ′-particles becomes weaker after annealing at 1270 $^{\circ}$C for 15 min. (e) shows a treasure map locating the optimized heat treatment parameters (yellow region with red star).

2.3. Stress/strain and microstructural characterization

After our newly designed sub-solvus solutionizing heat treatment, the γ′-particles in the IRs are about 200 - 300 nm in edge length, bigger than those in the DCs (~100 nm). The γ channels in the IRs widens to ~30 nm, also wider than those in the DCs (only a few nm). No contrast remains between the DCs and IRs in the WDS maps of the FZ. The element maps of W, Al, and Ti displayed in Figure 4b indicate no detectable chemical inhomogeneity. The equivalent strain map in Figure 4c reveals directly that the lattice strain in the interfacial region, where the strain is high and inhomogeneous in the as-printed state, becomes low and uniform. Detailed analysis shows that the equivalent strain has a nearly constant magnitude at about 0.5×10^{-3}, which is roughly the lower-bound measurement limit of the μXRD technique. The dislocations still show a distribution that is moderately non-uniform, after sub-solvus heat treatment. The DCs become almost dislocation free, with only 2 dislocations in the observed area (Figure 4e). But in the IRs, the dislocation density is higher (5×10^{13} m^{-2}) and more inhomogeneous, as observed in Figure 4f. From other TEM images taken in the same specimen, the dislocation density is in a range from 3×10^{13} m^{-2} to 1×10^{14} m^{-2}.
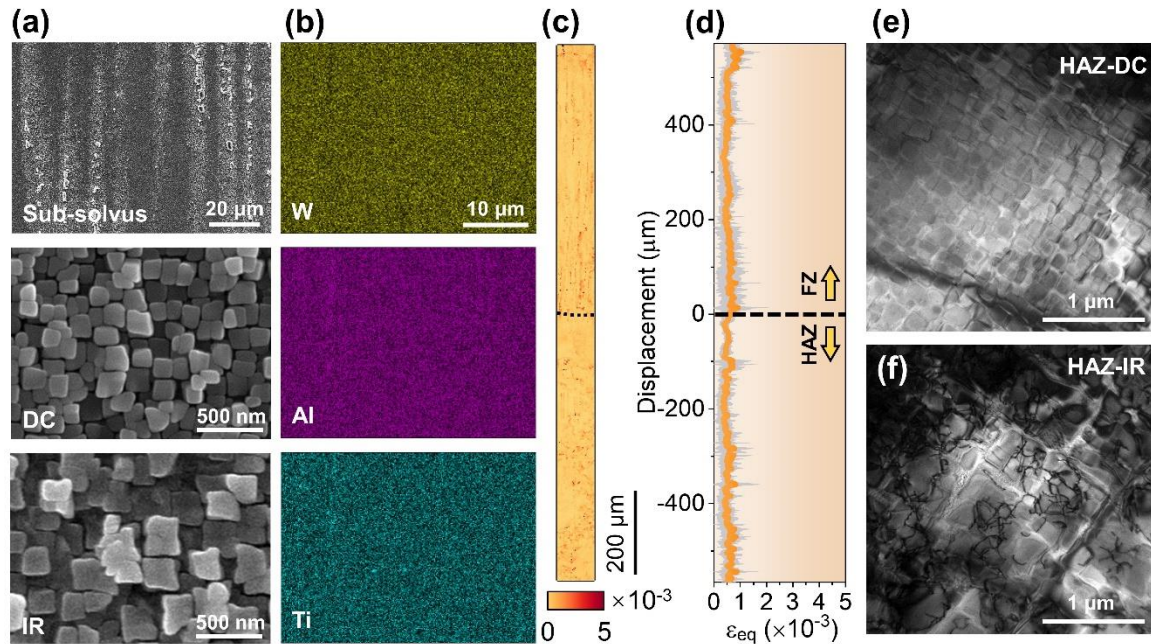
Figure 4 Microstructure after the sub-solvus solutionizing of the AM3 superalloy single crystal. The distributions of (a) element and (b-c) equivalent strain become homogeneous, although (d) dislocation densities in the DC and IR are different.

From the results above, we conclude that all the four **RASH** challenges are resolved via the single step of sub-solvus solutionizing treatment. That is, the stored deformation energy is released, recrystallization is avoided, stray grain growth is suppressed, and the chemical distribution is homogenized. What is to be dealt with next, is the morphology of the γ′-particles that subsequently evolve during ageing, and the remaining (left-over) dislocation contents. After the sub-solvus solutionizing treatment at 1270 ^{o}C for 15 min, the electron-beam-printed AM3 single crystal is aged following the standard heat treatment protocol to evolve the γ′-particles. In the DCs, regular cuboidal γ′-particles with the side length of 450 nm are obtained in both FZ and HAZ, and recovery reduces the dislocation density (Figure 5a and b) to less than 1% of that in the as-printed single crystals, and only individual dislocation can be detected occasionally. However, inside the IRs the microstructure is not fully uniform. In the IRs in FZ, γ′-particles coarsen

15

299 moderately, and dislocations are observed to align parallel to the γ/γ′ phase boundaries

300 (Figure 5c). The dislocation density in this region is 5×10^{13} m^{-2}, about 10 times lower

301 than that in the as-printed state while 10 times higher than that in the DCs. In the IRs in

302 HAZ, directional coarsening, *i.e.* rafting, of γ′-precipitates occurs, similar to what has

303 been observed at the early stage of creep test when γ′-precipitates are not well connected

304 and thus γ-γ′ topological phase inversion has not yet set in. From the bright-field TEM

305 image in Figure 5d, the γ′-precipitates are embraced by dislocations; this is because the

306 majority of the dislocations trying to recover are blocked effectively by the strengthening

307 precipitates, while only a small proportion of dislocations penetrate into γ′-precipitates.

308 The dislocation density in this region is measured to be approximately 10^{14} m^{-2}, higher

309 than that in the IRs of FZ but still 5 times lower than that in the as-printed single crystals.

310 The microstructure distributions of the γ′-particles of the fully heat treated laser 3D-

311 printed superalloys (Figure S4 in Supporting Information) are quite similar to those in the

312 electron beam melted one.
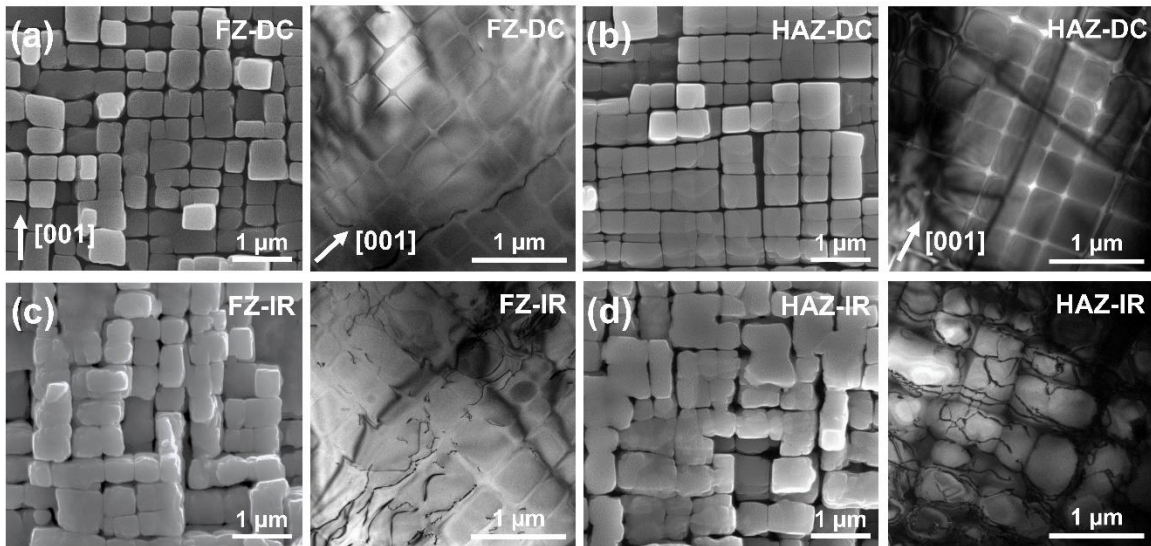
313

314 Figure 5 Microstructure of fully heat treated AM3 superalloy single crystal. γ′-precipitates in the DCs of (a)
315 FZ and (b) HAZ are uniform and dislocations are completely annihilated. Coarsening of γ′-precipitates in
316 the IRs of (c) FZ and (d) HAZ occurs and dislocations tend to reside along the γ/γ′ interface.

317

It must be noticed that the size and/or morphology of the γ′-particles in the fully

conventionally heat-treated cast superalloys are not completely homogeneous either [45],

mainly because the dendrite widths of cast superalloys are on the order of hundreds of

microns such that the chemical composition from the DCs to the IRs cannot be

homogenized even when the solutionizing heat treatment is carried out above the solvus

temperature. Therefore, the minor inhomogeneity resulted from our novel sub-solvus heat

treatment is believed to be acceptable. More details about this inhomogeneity will be
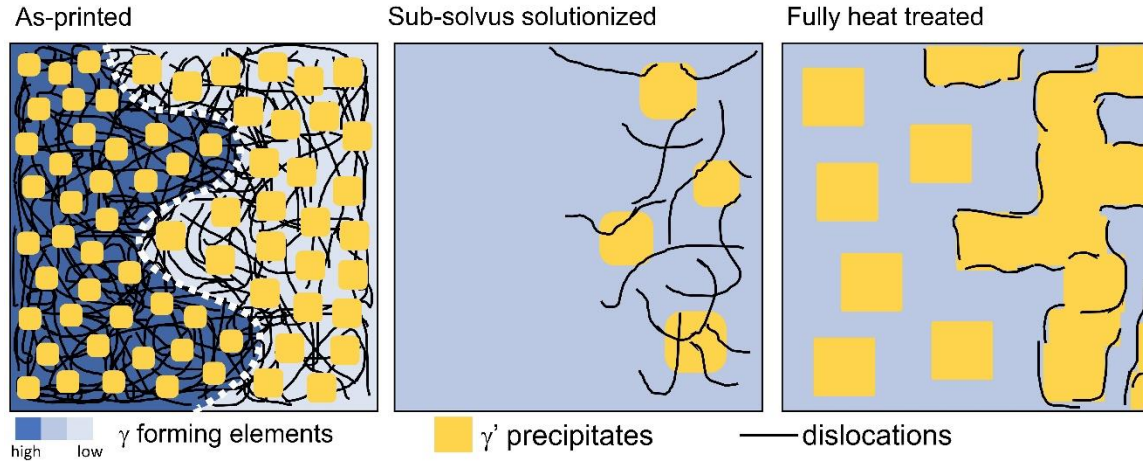
discussed further in the next section.

326

3. Discussion

Cracking is known to be one of the difficulties facing 3D-printed Ni-based

superalloys, it is also noticed that in most cases cracks occur along with the high-angle

grain boundaries. In other words, cracking is more frequently observed in polycrystalline

superalloys [46,47]. For superalloy single crystals, cracks are also observed when the

orientation is not perfectly controlled [33,48]. As reported previously [47], in the first few

layers of 3D-printing deposition of superalloy on a polycrystalline stainless steel base

metal, the as-printed superalloy inherits the crystal orientation of the base metal, and

cracks are detected along with the high-angle grain boundaries. As more layers are

cladded, [001] preferred orientation overwhelms, and eventually a single crystal is

obtained. In the meanwhile, no more cracks exist in the single crystal parts. In our current

study, a single crystal superalloy is employed as the base metal; therefore no cracks are

observed in the printed and melted superalloys with both laser and electron beam as the

17

340 heat source. Minor porosity is observed in the 3D-printed superalloy single crystals,

341 which leads to the concentration of strain/stress. But due to the small size of the pores in

342 the 3D-printed superalloys observed in this study (Figure S5 in Supporting Information)

343 and reported in previous literatures [7], as well as the recovery effect of the sub-solvus

344 treatment, no recrystallization is caused due to the porosity.

345 Post 3D-printing heat treatment, as one of the most effective approaches to tune the

346 microstructure and thus mechanical properties of superalloys, has attracted a lot of

347 attention. Because of the fine dendritic structures, shortening the heat treatment time has

348 been proposed; however, the solutionizing temperatures in previous reports are still

349 higher than the solvus of γ'-precipitates, under either ambient or high pressures [13,14]. This

350 is because in many of these previous investigations the 3D-printed superalloys are

351 polycrystalline, and thus recrystallization is acceptable. For 3D-printed single crystals,

352 **RASH** issues pose major challenges – low temperature for short time leads to

353 inhomogeneous chemical distribution, while high temperature (higher than 1320 $^{\circ}$C for

354 example) for even very short time may still trigger recrystallization. Exploiting the fact

355 that the presence of γ'-particles can impede the motion of dislocations and high-angle

356 grain boundaries, we have designed a novel heat treatment approach to achieve plastic

357 deformation recovery and chemical homogenization with a single annealing step.

358 Different from the previously employed super-solvus solutionizing heat treatment, which

359 just adopts the solutionizing temperature from the standard heat treatment protocol

360 established for the cast superalloys, the solutionizing temperature is optimized in a two-

361 step manner: firstly measuring the solvi of γ'-particles in DCs and IRs, and then further

362 specifying the critical temperature that does not induce recrystallization and stray grain

18

363   growth.

364   We now take a closer look at the mechanisms as to how the ***RASH*** issues are

365   resolved. As illustrated in Figure 6, a high-density of dislocations, non-uniform chemical

366   composition, and non-identical γ′-particle size/morphology are formed in the as-printed

367   superalloys, although the non-uniformity is the most obvious at locations on the surface.

368   When the temperature is elevated to above the solvus temperature (1280 ^{o}C for the AM3

369   superalloy single crystal in this report) of the DCs but below the IRs, atomic diffusion

370   easily covers half of the dendrite width (only a distance of 10 μm or less in 3D-printed

371   superalloys), to achieve compositional homogeneity. Since the γ′-particles in the DCs are

372   totally dissolved, dislocations move readily without obstacles to mediate recovery. In the

373   IRs, although the much wider γ-channels provide a spatial playground for dislocations to

374   interact with one another, γ′-particles in these regions are not fully dissolved and the

375   remnants impede the motion of dislocations and high-angle grain boundaries. This is why

376   the dislocation density is brought down effectively and meanwhile recrystallization is

377   largely avoided and stray grain growth is suppressed. These left-over dislocations and

378   their associated deformation energy, during the aging heat treatment, provide the driving

379   force for γ′-particle growth, which is similar to rafting during creep, except that the

380   residual strain/stress caused by the dislocations is more inhomogeneous in both

381   magnitude and direction on the microscopic scale, such that the γ′-particle coarsening is

382   less directional than that in a conventional creep test.

| As-printed | Sub-solvus solutionized | Fully heat treated |

γ forming elements   high low   γ' precipitates   ——— dislocations

Figure 6 Evolution of γ′-precipitate size/morphology and dislocation density/configuration during the sub-solvus solutionizing and subsequent aging heat treatment. Light and dark blue colors in the as-printed state indicate chemical inhomogeneity, which is homogenized after heat treatment.

An interesting question is whether it is possible, and how, to further enhance the homogeneity. It is obvious that elevating the solutionizing heat treatment temperature would promote the homogeneity of the size and morphology of γ′-precipitates, because recovery would be more thorough, leaving less dislocations and lower residual strain/stress after sub-solvus solutionizing treatment. However, higher solutionizing temperature also increases the likelihood for recrystallization and stray grain growth, especially the latter. As we observed, stray grains grow bigger significantly at 1276 $^{\circ}$C after annealing for 15 minutes (Figure 3c). Consequently, we conclude that while the compositional homogeneity is relatively easy to achieve, the γ′-morphology homogeneity is counter-balanced by the risk of forming high-angle grain boundaries that are prone to migration. This trade-off could lead to an optimized solutionizing temperature. As for treatment durations, systematic investigation shows that extending the annealing time to 30 min leads to even more severe γ′-coarsening (Figure S6). Reducing the annealing time to 10 min or even shorter exposes the 3D-printed superalloys to the risk of inhomogeneity

402   in chemical composition. By balancing all these factors, we determined the heat treatment

403   parameters to be 1270 $^{\circ}$C for 15 min.

404   How much the non-uniform γ′-precipitates in the IRs would influence the high-

405   temperature mechanical properties of the superalloy single crystal is of interest. To

406   quantify the effects would require extensive future research but a rough estimate can be

407   made here. It has been reported that the high temperature creep properties of crept

408   superalloy single crystal René 5 could be restored by 82 − 85%, compared to the cast

409   René 5 superalloy, by means of rejuvenation heat treatment with solutionizing at the

410   temperature 28 $^{\circ}$C below the solvus and then standard aging [6]. Although in this reference

411   paper, no detailed γ′ microstructure evolution during the creep test and rejuvenation was

412   reported, it was believed that solutionizing at 28 $^{\circ}$C below solvus must have resulted in an

413   incomplete recovery, and thus rafted γ′-precipitates. In our study, the solutionizing

414   temperature is only 10 $^{\circ}$C below the solvus of the γ′-precipitates in IRs, so the coarsening

415   is much more moderate. Therefore, we expect the creep properties of the superalloy

416   single crystals after the novel heat treatment protocol to be at least better than 85% of

417   their cast counterparts after full heat treatment.

418   We note that the one-step annealing strategy to tackle the ***RASH*** issues reported in

419   this study can be applicable to a variety of 3D-printed superalloys. As demonstrated in

420   Figure S6 in Supporting Information, our heat treatment is successful for both laser and

421   electron beam 3D-printed (or melted) AM3 superalloy single crystals. Laser 3D-printed

422   SRR99 single crystal has also been tested (Figure S7), with the same outcome when it

423   comes to accomplishing ***RASH***.

424   Finally, the simplicity and efficiency are appealing attributes of our new one-step

425 annealing approach. Compared to the previous "recovery annealing plus standard heat

426 treatment", both time and energy consumption are markedly reduced, shortening the

427 processing chain and reducing the associated costs and wasted parts. More importantly,

428 the existing stray grains, which are unavoidable due to the nature of 3D printing, do not

429 coarsen with this sub-solvus solutionizing heat treatment. Since the service temperature

430 of the single crystal blades will be lower than the solutionizing treatment temperature, we

431 expect the stray grains to be stable during service. Our method also offers a double

432 insurance in case there are occasionally some tiny stray grains leftover on the surface

433 after post-printing machining or etching.

434

435 ## 4. Conclusion

436 In summary, we have designed a new heat treatment protocol to release stored

437 deformation energy, avoid recrystallization, suppress stray grain growth, and homogenize

438 the chemical and microstructure distribution, all of which are mandated for 3D-printing

439 manufacture and repair of Ni-based superalloy single crystals. It is remarkable that the

440 multiple **RASH** requirements are satisfied all at once, via a single-step sub-solvus

441 solutionizing treatment. Specifically, as ultra-fine dendrite width is generated by the steep

442 temperature gradient of the 3D-printing process, the necessary distance for diffusion to

443 cover is greatly reduced, making sub-solvus annealing adequate to accomplish chemical

444 homogenization. Meanwhile, by setting the heat treatment temperature between the

445 solvus points of DCs and IRs, the dislocations move freely in the DCs to annihilate fully,

446 eliminating the stored energy that drives the nucleation of recrystallizing new grains,

447 while the remaining precipitates in the IRs are able to hinder the motion and interactions

448   of dislocations, the nucleation of recrystallization and the migration of stray grain

449   boundaries. Meanwhile, our experiments and diffusion analysis successfully singled out

450   an annealing time that is sufficiently long to homogenize the chemical species

451   distribution, while as short as possible to limit the γ'-particle coarsening in the

452   undissolved IRs. Via the construction of a temperature-time "treasure map", 1270 $^{\circ}$C for

453   15 min is found to be the "sweet spot" for optimal solutionizing to resolve the **RASH**

454   issues. Such a tactfully crafted heat treatment thus provides a much-needed stepping

455   stone, for making 3D printing practical to the manufacture and repair of single-crystal

456   superalloy parts, as exemplified above by the AM3 superalloy single crystals 3D-printed

457   using either electron or laser beams, including those with leftover surface stray grains.

Materials and methods

In this study, three types of superalloy single crystals were investigated, which were electron beam melted AM3, laser 3D-printed AM3, and laser 3D-printed SRR99. The nominal compositions of AM3 and SRR99 are Ni-7.82Cr-5.34Co-2.25Mo-4.88W-6.02Al-1.94Ti-3.49Ta and Ni-8.39Cr-5.01Co-9.47W-5.47Al-2.14Ti-2.92Ta in weight percentage, respectively. The [001] cast AM3/SRR99 single crystal base-metal boules were cut into cylinders ~4 mm in height. Electron beam melting with no feedstock was carried out using a DMAMS Zcomplex3^{TM} electron-beam 3D-printing system operated in 10^{-3} mbar vacuum. Electron beam of 15 mA was accelerated to 60 keV and focused onto the base metal surface to form a melt pool. Line scanning was programmed with the velocity of 10 mm/s to ensure epitaxial dendrite growth in the melt pool. A FZ of about 1500 μm in width and 800 μm in depth was generated. Laser 3D-printing was conducted on an in-house developed co-axial laser cladding apparatus equipped with a CO_2 laser with the beam size of 2 mm. The gas atomized superalloy powders with diameters ranging from 48 to 180 μm with similar composition to the base metal were coaxially injected at a 11 g/min feeding speed by high-purity Ar gas carrier into the molten pool formed by the laser beam with a power of 2000 W and 2 mm/s laser scanning speed. The interlayer spacing is 0.2 mm with a back-and-forth scan path. Therefore the molten powder solidified on top of the crystal and deposited layer by layer. More detailed information about the manufacturing process can be found elsewhere [49].

In our novel heat treatment protocol with sub-solvus solutionizing, the electron beam melted and laser 3D-printed single crystal superalloys were first solutionized at sub-solvus temperature and then aged at 1100 ^{o}C and 870 ^{o}C for 6 h and 20 h, respectively.

481 The optimized solutionizing condition was optimized to be 1270 $^{\circ}$C for 15 min.

482 Comparisons were made with identical electron beam melted and laser 3D-printed

483 samples, heat treated via two other protocols. The "standard heat treatment" was carried

484 out in a similar manner as the sub-solvus heat treatment, except that the solutionizing

485 treatment was at 1300 $^{\circ}$C. Note that the duration of the so-called standard solutionizing

486 heat treatment was significantly shorter than that in the superalloy handbook, because of

487 the narrow dendrite width. The last heat treatment process involves a recovery annealing

488 step at 1100 $^{\circ}$C for 6 h, prior to the standard heat treatment. The heating rate of all

489 specimens was set at 15 $^{\circ}$C/min. All the heat treatment experiments were performed using

490 a CARBOLITE® RHF 1500 muffle furnace, equipped with an R-type thermocouple

491 installed at the center of the back inside wall of the furnace chamber to monitor the

492 temperature. In order to verify the accuracy of the temperature, an AM3 cast superalloy

493 single crystal was firstly solutionized at 1300 $^{\circ}$C for 3 h and then annealed at

494 temperatures from 1260 to 1280 $^{\circ}$C for 30 min, respectively. Observed from the

495 secondary electron images taken in the scanning electron microscopy, the solvus

496 temperature of the γ′-precipitates in the DCs was measured to be between 1260 to 1280

497 $^{\circ}$C (Figure S8 in Supporting Information), which is in agreement with the literature [39]. All

498 samples were air cooled at the rate of approximately 300 $^{\circ}$C/min once the heat treatment

499 was finished.

500 The microstructure was examined under secondary electron mode in a SEM after

501 etching in 25% phosphoric acid water solution at the voltage of 5 V for 10 s. WDS for

502 element distribution study was conducted in a SuperProbe JXA-8230 Electron Probe

503 Microanalyzer at the accelerating voltage of 20 kV. EBSD was carried out after the

504   sample surface was polished electrochemically in 10% perchloric acid alcohol solution at

505   the voltage of ~30 V for 60 s. All TEM images displayed in this manuscript were taken in

506   a JEM-2100F field emission electron microscope at the accelerating voltage of 200 kV.

507   μXRD sample was electro-polished in the same way, and then scanned using micro-

508   focused synchrotron polychromatic X-ray beam on Beamline 12.3.2 at the Advanced

509   Light Source of Lawrence Berkeley National Laboratory [50]. The collected Laue

510   diffraction data were processed using a custom-developed software based on the peak

511   position comparison method to measure [51] and visualize [52] the strain distribution

512   accurately. Diffraction peaks were searched based on a user-defined peak to background

513   threshold and fitted using a 2D Lorentzian function to obtain the peak position precisely.

514   By comparing the angles between experimentally measured diffraction peak positions

515   with the theoretically calculated ones, the strain tensor and thus the equivalent strain are

516   calculated. TEM specimens were prepared using the conventional twin-jet

517   electropolishing.

Author contributions

K.C. designed the project in consultation with E.M. S.L. conducted the experiments and electron microscopy characterization. W.H. provided the additive-manufactured and re-melted specimens. Y.L. and S.L. analyzed and interpreted the μXRD data under the supervision of K.C. and N.T. K.C. and E.M. wrote the paper based on the draft from S.L. All authors contributed to the discussions of the results.

References:

1. Pollock, T. M. Alloy design for aircraft engines. *Nat. Mater.* **15**, 809 (2016).

2. Srivastava, R. R., Kim, M. S., Lee, J. C., Jha, M. K. & Kim, B. S. Resource recycling of superalloys and hydrometallurgical challenges. *J. Mater. Sci.* **49**, 4671–4686 (2014).

3. Carter, P., Cox, D. C., Gandin, C. A. & Reed, R. C. Process modelling of grain selection during the solidification of single crystal superalloy castings. *Mater. Sci. Eng. A* **280**, 233–246 (2000).

4. DebRoy, T. *et al.* Scientific, technological and economic issues in metal printing and their solutions. *Nat. Mater.* **18**, 1026–1032 (2019).

5. Panwisawas, C., Tang, Y. T. & Reed, R. C. Metal 3D printing as a disruptive technology for superalloys. *Nat. Commun.* **11**, 2327 (2020).

6. Rettberg, L. H., Callahan, P. G., Goodlet, B. R. & Pollock, T. M. Rejuvenation of Directionally Solidified and Single-Crystal Nickel-Base Superalloys. *Metall. Mater. Trans. A Phys. Metall. Mater. Sci.* **52**, 1609–1631 (2021).

7. Körner, C. *et al.* Microstructure and Mechanical Properties of CMSX-4 Single Crystals Prepared by Additive Manufacturing. *Metall. Mater. Trans. A Phys. Metall. Mater. Sci.* **49**, 3781–3792 (2018).

8. Liang, Y. J., Cheng, X., Li, J. & Wang, H. M. Microstructural control during laser additive manufacturing of single-crystal nickel-base superalloys: New processing–microstructure maps involving powder feeding. *Mater. Des.* **130**, 197–207 (2017).

9. Basak, A., Acharya, R. & Das, S. Additive Manufacturing of Single-Crystal Superalloy CMSX-4 Through Scanning Laser Epitaxy: Computational Modeling,

558   Experimental Process Development, and Process Parameter Optimization. *Metall.*

559   *Mater. Trans. A Phys. Metall. Mater. Sci.* **47**, 3845–3859 (2016).

560   10.   Chen, K. *et al.* Rafting-Enabled Recovery Avoids Recrystallization in 3D-Printing-

561   Repaired Single-Crystal Superalloys. *Adv. Mater.* **32**, 1–8 (2020).

562   11.   Bürger, D., Parsa, A. B., Ramsperger, M., Körner, C. & Eggeler, G. Creep

563   properties of single crystal Ni-base superalloys (SX): A comparison between

564   conventionally cast and additive manufactured CMSX-4 materials. *Mater. Sci. Eng.*

565   *A* **762**, 138098 (2019).

566   12.   Lopez-Galilea, I. *et al.* Additive manufacturing of CMSX-4 Ni-base superalloy by

567   selective laser melting: Influence of processing parameters and heat treatment.

568   *Addit. Manuf.* **30**, 100874 (2019).

569   13.   Ramsperger, M. *et al.* Solution Heat Treatment of the Single Crystal Nickel-Base

570   Superalloy CMSX-4 Fabricated by Selective Electron Beam Melting. *Adv. Eng.*

571   *Mater.* **17**, 1486–1493 (2015).

572   14.   Ruttert, B. *et al.* Impact of hot isostatic pressing on microstructures of CMSX-4

573   Ni-base superalloy fabricated by selective electron beam melting. *Mater. Des.* **110**,

574   720–727 (2016).

575   15.   Reed, R. C. & Rae, C. M. F. Physical Metallurgy of the Nickel-Based Superalloys.

576   in *Physical Metallurgy: Fifth Edition* (eds. David E, L. & Hono, K.) vol. 3 2215–

577   2290 (Elsevier B.V., 2014).

578   16.   Reed, R. C. *Superalloy fundamentals and applications*. (Cambridge University

579   Press, 2006).

580   17.   Körner, C. Additive manufacturing of metallic components by selective electron

581   beam melting - A review. *Int. Mater. Rev.* **61**, 361–377 (2016).

582   18.   Zhang, Y. *et al.* Additive Manufacturing of Metallic Materials: A Review. *J.*

583   *Mater. Eng. Perform.* **27**, 1–13 (2018).

584   19.   Yap, C. Y. *et al.* Review of selective laser melting: Materials and applications.

585   *Appl. Phys. Rev.* **2**, 041101–1 (2015).

586   20.   Gäumann, M., Bezençon, C., Canalis, P. & Kurz, W. Single-crystal laser

587   deposition of superalloys: Processing-microstructure maps. *Acta Mater.* **49**, 1051–

588   1062 (2001).

589   21.   Wang, G. *et al.* Effects of scanning speed on microstructure in laser surface-melted

590   single crystal superalloy and theoretical analysis. *J. Mater. Sci. Technol.* **34**, 1315–

591   1324 (2018).

592   22.   Kearsey, R. M., Beddoes, J. C., Jones, P. & Au, P. Compositional design

593   considerations for microsegregation in single crystal superalloy systems.

594   *Intermetallics* **12**, 903–910 (2004).

595   23.   Liang, Y. J. & Wang, H. M. Origin of stray-grain formation and epitaxy loss at

596   substrate during laser surface remelting of single-crystal nickel-base superalloys.

597   *Mater. Des.* **102**, 297–302 (2016).

598   24.   Anderson, T. D., DuPont, J. N. & DebRoy, T. Origin of stray grain formation in

599   single-crystal superalloy weld pools from heat transfer and fluid flow modeling.

600   *Acta Mater.* **58**, 1441–1454 (2010).

601   25.   R. Bürgel, P. D. Portella & J. Preuhs. Recrystallization in single crystal of nickel

602   base superalloy. in *superalloys 2000* (eds. Pollock, T. M. & Kissinger, R. D.) 229–

603   238 (TMS, 2000).

604   26.   Kuipers, J., Wiens, K. & Ruggiero, B. Rejuvenation heat treatment of single

605   crystal gas turbine blades. *Proc. ASME Turbo Expo* **6**, 1–9 (2017).

606   27.   Fuchs, G. E. & Boutwell, B. A. Modeling of the partitioning and phase

607   transformation temperatures of an as-cast third generation single crystal Ni-base

608   superalloy. *Mater. Sci. Eng. A* **333**, 72–79 (2002).

609   28.   Cheng, K. Y., Jo, C. Y., Jin, T. & Hu, Z. Q. Influence of applied stress on the γ′

610   directional coarsening in a single crystal superalloy. *Mater. Des.* **31**, 968–971

611   (2010).

612   29.   Reed, R. C., Cox, D. C. & Rae, C. M. F. Kinetics of rafting in a single crystal

613   superalloy: Effects of residual microsegregation. *Mater. Sci. Technol.* **23**, 893–902

614   (2007).

615   30.   Brückner, U., Epishin, A., Link, T. & Dressel, K. The influence of the dendritic

616   structure on the γ/γ′-lattice misfit in the single-crystal nickel-base superalloy

617   CMSX-4. *Mater. Sci. Eng. A* **247**, 23–31 (1998).

618   31.   Milhet, X., Arnoux, M., Cormier, J., Mendez, J. & Tromas, C. On the influence of

619   the dendritic structure on the creep behavior of a Re-containing superalloy at high

620   temperature/low stress. *Mater. Sci. Eng. A* **546**, 139–145 (2012).

621   32.   Gorsse, S., Hutchinson, C., Gouné, M. & Banerjee, R. Additive manufacturing of

622   metals: a brief review of the characteristic microstructures and properties of steels,

623   Ti-6Al-4V and high-entropy alloys. *Sci. Technol. Adv. Mater.* **18**, 584–610 (2017).

624   33.   Chauvet, E. *et al.* Hot cracking mechanism affecting a non-weldable Ni-based

625   superalloy produced by selective electron Beam Melting. *Acta Mater.* **142**, 82–94

626   (2018).

627   34.   Li, Y. *et al.* Multi-scale microstructural investigation of a laser 3D printed Ni-

628   based superalloy. *Addit. Manuf.* **34**, 101220 (2020).

629   35.   Vilaro, T., Colin, C., Bartout, J. D., Nazé, L. & Sennour, M. Microstructural and

630   mechanical approaches of the selective laser melting process applied to a nickel-

631   base superalloy. *Mater. Sci. Eng. A* **534**, 446–451 (2012).

632   36.   Ramsperger, M., Singer, R. F. & Körner, C. Microstructure of the Nickel-Base

633   Superalloy CMSX-4 Fabricated by Selective Electron Beam Melting. *Metall.*

634   *Mater. Trans. A Phys. Metall. Mater. Sci.* **47**, 1469–1480 (2016).

635   37.   Hegde, S. R., Kearsey, R. M. & Beddoes, J. C. Designing homogenization-solution

636   heat treatments for single crystal superalloys. *Mater. Sci. Eng. A* **527**, 5528–5538

637   (2010).

638   38.   Yu, J. *et al.* Effect of heat treatment on microstructure and stress rupture life of

639   DD32 single crystal Ni-base superalloy. *Mater. Sci. Eng. A* **460–461**, 420–427

640   (2007).

641   39.   Steuer, S. *et al.* Creep behavior under isothermal and non-isothermal conditions of

642   AM3 single crystal superalloy for different solutioning cooling rates. *Mater. Sci.*

643   *Eng. A* **601**, 145–152 (2014).

644   40.   Murray, S. P. *et al.* A Defect-Resistant Co-Ni Superalloy for 3D Printing. *Nat.*

645   *Commun.* **11**, 4975 (2020).

646   41.   Norfleet, D. M., Dimiduk, D. M., Polasik, S. J., Uchic, M. D. & Mills, M. J.

647   Dislocation structures and their relationship to strength in deformed nickel

648   microcrystals. *Acta Mater.* **56**, 2988–3001 (2008).

649   42.   Barabash, O. M. *et al.* Evolution of dislocation structure in the heat affected zone

650   of a nickel-based single crystal. *J. Appl. Phys.* **96**, 3673–3679 (2004).

651   43. Karunaratne, M. S. A., Cox, D. C., Carter, P. & Reed, R. C. Modelling of the

652   Microsegregation in CMSX-4 Superalloy and its Homogenisation During Heat

653   Treatment. in *superalloys 2000* (eds. Pollock, T. M. & Kissinger, R. D.) 263–272

654   (TMS, 2000).

655   44. Cardoso, J. A. S. B., Almeida, A. & Vilar, R. Microstructure of a coated single

656   crystalline René N5 part repaired by epitaxial laser deposition. *Addit. Manuf.* **49**,

657   102515 (2022).

658   45. Su, X. *et al.* Microstructural evolution and compositional homogenization of a low

659   Re-bearing Ni-based single crystal superalloy during through progression of heat

660   treatment. *Mater. Des.* **141**, 296–322 (2018).

661   46. Kontis, P. *et al.* Atomic-scale grain boundary engineering to overcome hot-

662   cracking in additively-manufactured superalloys. *Acta Mater.* **177**, 209–221 (2019).

663   47. Ramsperger, M. & Körner, C. Selective electron beam melting of the single

664   crystalline nickel-base superalloy CMSX-4®: From columnar grains to a single

665   crystal. in *Superalloys 2016* (eds. Mark, H. et al.) 341–349 (TMS, 2016).

666   48. Chauvet, E., Tassin, C., Blandin, J. J., Dendievel, R. & Martin, G. Producing Ni-

667   base superalloys single crystal by selective electron beam melting. *Scr. Mater.* **152**,

668   15–19 (2018).

669   49. Ci, S., Liang, J., Li, J., Zhou, Y. & Sun, X. Microstructure and tensile properties of

670   DD32 single crystal Ni-base superalloy repaired by laser metal forming. *J. Mater.*

671   *Sci. Technol.* **45**, 23–34 (2020).

672   50. Kunz, M. *et al.* A dedicated superbend x-ray microdiffraction beamline for

673   materials, geo-, and environmental sciences at the advanced light source. *Rev. Sci.*

674   *Instrum.* **80**, 035108 (2009).

675   51.   Kou, J., Chen, K. & Tamura, N. A peak position comparison method for high-

676   speed quantitative Laue microdiffraction data processing. *Scr. Mater.* **143**, 49–53

677   (2018).

678   52.   Li, Y. *et al.* XtalCAMP: A comprehensive program for the analysis and

679   visualization of scanning Laue X-ray micro-/nanodiffraction data. *J. Appl.*

680   *Crystallogr.* **53**, 1392–1403 (2020).

681